arXiv:0709.1580v1 [astro-ph] 11 Sep 2007

Suzaku Detection of Extended/Diffuse Hard X-Ray Emission from the Galactic Center

Takayuki Yuasa,[1] Ken-ichi Tamura,[2,1] Kazuhiro Nakazawa,[1] Motohide Kokubun,[2] Kazuo Makishima,[1,3]
Aya Bamba,[2] Yoshitomo Maeda,[2] Tadayuki Takahashi,[2,1] Ken Ebisawa,[2,1] Atsushi Senda,[3]
Yoshiaki Hyodo,[4] Takeshi Go Tsuru,[4] Katsuji Koyama,[4] Shigeo Yamauchi,[5] Hiromitsu Takahashi[6]

[1]*Department of Physics, School of Science, University of Tokyo, 7-3-1 Hongo, Bunkyo-ku, Tokyo 113-0033*
[2]*Department of High Energy Astrophysics, Institute of Space and Astronautical Science (ISAS),*
Japan Aerospace Exploration Agency (JAXA), 3-1-1 Yoshinodai, Sagamihara, Kanagawa 229-8510
[3]*Cosmic Radiation Laboratory, The Institute of Physical and Chemical Research (RIKEN), 2-1 Hirosawa, Wako, Saitama 351-0198*
[4]*Department of Physics, Graduate School of Science, Kyoto University, Kita Shirakawa Oiwake-cho, Sakyo-ku, Kyoto 606-8502*
[5]*Faculty of Humanities and Social Sciences, Iwate University, 3-18-34 Ueda, Morioka, Iwate 020-8550*
[6]*Department of Physical Science, Hiroshima University, 1-3-1 Kagamiyama, Higashi-Hiroshima, Hiroshima 739-8526*
yuasa@amalthea.phys.s.u-tokyo.ac.jp

Abstract

Five on-plane regions within $\pm 0°\!\!.8$ of the Galactic center were observed with the Hard X-ray Detector (HXD) and the X-ray Imaging Spectrometer (XIS) onboard Suzaku. From all regions, significant hard X-ray emission was detected with HXD-PIN up to 40 keV, in addition to the extended plasma emission which is dominant in the XIS band. The hard X-ray signals are inferred to come primarily from a spatially extended source, rather than from a small number of bright discrete objects. Contributions to the HXD data from catalogued X-ray sources, typically brighter than 1 mCrab, were estimated and removed using information from Suzaku and other satellites. Even after this removal, the hard X-ray signals remained significant, exhibiting a typical 12–40 keV surface brightness of 4×10^{-10} ergs cm^{-2} s^{-1} deg^{-2} and power-law-like spectra with a photon index of 1.8. Combined fittings to the XIS and HXD-PIN spectra confirm that a separate hard tail component is superposed onto the hot thermal emission, confirming a previous report based on the XIS data. Over the 5–40 keV band, the hard tail is spectrally approximated by a power law of photon index ~ 2, but better by those with somewhat convex shapes. Possible origins of the extended hard X-ray emission are discussed.

Key words: Galaxy: center — X-rays: diffuse background

1. Introduction

Extended X-ray emission associated with our Galaxy has been observed for more than 20 years (Worrall et al. 1982; Iwan et al. 1982; Warwick et al. 1985; Koyama et al. 1986), and has been revealed to consist of three distinct spatial components; the Galactic ridge component (Koyama et al. 1986; Kaneda et al. 1997), the Galactic bulge components (Yamauchi & Koyama 1993; Kokubun 2001), and the Galactic center (GC) component discovered with Ginga (Koyama et al. 1989; Yamauchi et al. 1990). Over a typical energy range of $2-10$ keV, all the three emission components are spectrally dominated by thermal emission from hot plasmas with a temperature of $\sim 10^8$ K, as evidenced by strong K-shell emission lines from highly ionized iron in the spectra (Koyama et al. 1986; Yamauchi & Koyama 1993; Kaneda et al. 1997; Kokubun 2001).

The overall phenomenon has been interpreted either as truly diffuse emission permeating the interstellar space (Sugizaki et al. 2001; Ebisawa et al. 2001), or as superposition of a large number of unresolved discrete (mostly point-like) X-ray sources, such as cataclysmic variables (CVs) and RS CVn type binaries (Revnivtsev et al. 2006). However, either interpretation has problems. If the emission is from truly diffuse plasma,

the measured temperature ($\sim 5 - 10$ keV) is inferred to significantly exceed the gravitational escape temperature of the Galaxy (~ 0.5 keV), and the pressure to significantly exceed that of any known interstellar energy component. If instead the plasma were escaping freely from the disk, a large input energy would be required to supply the plasma and to sustain the emission within the escaping time scale of the plasma of $\sim 10^5$ yr. The other scenario invoking discrete sources also has a serious difficulty, in that deep observations with Chandra resolved only $10 - 30\%$ of the total emission from the ridge (Ebisawa et al. 2001; Revnivtsev et al. 2007) and the GC (Muno et al. 2004) into point sources: to account for the remainder, a new class of much dimmer but more numerous X-ray point sources are needed.

A direct comparison of the emission spectra of the three spatial components with one another, and with those of the candidates of unresolved sources, will provide an important clue to the origin of the extended Galactic X-ray emission. Actually, the ridge and bulge emissions have been extensively studied in energies both below and above 10 keV, incorporating imaging (e.g., Kaneda et al. 1997) and collimated (e.g., Yamasaki et al. 1997; Kokubun 2001) instruments, respectively. As a result, the spectra of the X-ray emission filling these two regions have been confirmed to exhibit a clear spectral excess in high ener-

gies, or a hard tail, above the thermal emission (Yamasaki et al. 1997; Valinia & Marshall 1998; Valinia et al. 2000; Kokubun 2001). The excess has been taken as evidences for ongoing particle acceleration in the interstellar space (Yamasaki et al. 1997), or alternatively, for a significant population of numerous hard X-ray sources such as CVs (Revnivtsev et al. 2006).

In the GC region, the extended thermal emission has been studied extensively in energies below 10 keV (Sidoli et al. 1999; Muno et al. 2004), and the recent Suzaku X-ray Imaging Spectrometer (XIS) observations have revealed a strong spectral hard tail to accompany the GC emission as well (Koyama et al. 2007a). Nevertheless, its direct confirmation in energies above ~ 10 keV has so far been unavailable, because studies with collimated or coded-mask instruments are severely hampered by the high surface density of bright X-ray point sources around the GC.

The silicon PIN diodes (hereafter HXD-PIN) of the Hard X-ray Detector (HXD; Takahashi et al. 2007; Kokubun et al. 2007) onboard the Suzaku satellite (Mitsuda et al. 2007) has a tightly collimated field of view (FOV) of $34\prime \times 34\prime$ (FWHM) with the lowest detector background ever achieved, and enables to measure the hard tail component of the extended GC emission in energies above 10 keV, without being hampered by contamination of bright point sources. In fact, the solid angle of HXD-PIN is ~ 4.5 and ~ 2.5 times smaller than that of the BeppoSAX PDS and the RXTE HEXTE, respectively. In the present paper, we report on the HXD-PIN detection of apparently extended bright hard X-ray emission from the GC region.

2. Observation

We observed 5 different regions around the GC ($-0°.5 < l < +0°.5$) with the XIS and the HXD onboard Suzaku, in 2005 September and October, as well as in 2006 February, March and September, each for an exposure of $30-70$ ks. As listed in table 1, we hereafter call these observed regions A, B, C, D and E. Region A and B, the nearest two to the GC, were observed three times and twice respectively, so we distinguish those observations by putting subscripts.

In 2005 September, additional three short offset observations were conducted, to obtain information on known bright X-ray point sources that lie outside the XIS field of view but inside the PIN FOV during the relevant observations. These offset data allow us to estimate to what extent they contaminate the HXD data from regions A through E. The point sources targeted in the offset observations are 1A 1742$-$294, KS 1741$-$293 and 1E 1743.1$-$2843; the net exposure of the XIS for these point sources were 5.2 ks, 4.8 ks and 4.2 ks, respectively (table 1).

3. Data Reduction

The reduction and analysis of the present data were carried out using the HEADAS software version 6.1.2. The data produced by Suzaku Data Processing version 1.3 were analyzed. In the spectral fitting, we used `xspec` version 11.3. The utilized PIN response matrix file versions were 2006-08-09 and 2006-08-14 for uniform emission and a point source, respectively. The XIS response matrices and auxiliary response files were calculated using `xisrmfgen` and `xissimarfgen` (version 2006-11-26).

We removed the XIS and HXD data obtained while the elevation angle is less than 5° (ELV$< 5°$) and the spacecraft is in the South Atlantic Anomaly. Additionally, we imposed the condition that the day earth elevation angle is less than 20° (DYE_ELV$< 20°$) for the XIS data. The HXD data acquired in regions of low cutoff rigidity (COR< 8 GV) were also excluded.

In analyzing the HXD data, we extracted the signals from all 64 HXD-PIN detectors in each observation except for Region A_3. Because of a break-down like event in a silicon PIN detector which took place in 2006 May, the high voltage supplied to 16 PIN detectors (including that particular one) was changed from 500 V to 400 V. The third observation of Region A (Region A_3) was conducted after this operation. Because the response under the reduced high voltage is yet to be calibrated, we limited the present analysis of the A_3 data to signals from the other 48 PIN detectors, resulting in 25% reduction in the effective area. In the present study, we did not use the GSO data because of its lower signal to noise ratio than that of PIN by about an order of magnitude.

We estimated non X-ray background (NXB) of the XIS using night-earth data sorted by cut off rigidity. That of the HXD was estimated by a synthetic model (Kokubun et al. 2007), which mainly relies on the count rate of the PIN upper discriminator (i.e. count rate of cosmic ray particles) and utilizes night-earth data as background templates.

The GC region hosts a large number of discrete X-ray sources. In the following analysis, however, we did not remove any point sources, and extracted events from whole area of the XIS CCDs, excluding the corners illuminated by calibration radioisotope signals.

Figure 1 shows a mosaic image of the GC region, constructed from the five pointings, using $2-10$ keV data from all the four XIS CCDs. All the imaging area of the CCD chips is used, except for the two corners of each camera irradiated by calibration isotopes.

4. Analysis and Results

4.1. Light curves

Figure 2 shows light curves of the raw $10-40$ keV HXD-PIN count rates of Region A_1 and Region C, binned into the orbital period of the spacecraft, 5760 s. The modeled NXB and the NXB-subtracted count rates are also plotted. The raw counts were corrected for dead time fraction in each bin, which was calculated from the "pseudo-event" rates (Takahashi et al. 2007; Kokubun et al. 2007) as about $5-9\%$. The NXB counts (and hence the raw counts too) exhibit periodic variations due to activation in the South Atlantic Anomaly (SAA) and subsequent decays of the produced radioactive isotopes. Since the reproducibility of the NXB model decrease (overestimating the NXB counts) slightly when the satellite orbit crosses the SAA, the NXB-subtracted signal count rate in Region A_1 are also undulated around $(2-5) \times 10^4$ s. However in other time regions, it is rather constant within statistical errors.

We likewise confirmed that the NXB-subtracted signal counts of all other regions, except for that of Region C, are rather constant during the present observations. However, as

Table 1. Observations of the Galactic Center region.

Name	Sequence number	Position* l (°)	b (°)	Start (UTC)	Exp.† (ks)
Region A$_1$	100027010	0.06	0.07	2005-09-23 07:27	31.1
Region A$_2$	100037040	0.06	0.07	2005-09-30 07:43	33.3
Region A$_3$	100048010	0.06	0.07	2006-09-08 02:32	38.2
Region B$_1$	100027020	-0.25	0.05	2005-09-24 15:22	30.3
Region B$_2$	100037010	-0.25	0.05	2005-09-29 05:21	32.8
Region C	500005010	0.43	0.12	2006-03-27 23:48	71.7
Region D	100037060	0.64	0.10	2005-10-10 12:28	56.6
Region E	500018010	-0.57	0.09	2006-02-20 13:01	38.3

Name	Sequence number	Target Position‡ l (°)	b (°)	Start (UTC)	Exp.§ (ks)
Offset1_1 (1A 1742−294)	100027030	-0.441	-0.389	2005-09-24 12:06	2.0
Offset1_2 (1A 1742−294)	100037020	-0.441	-0.389	2005-09-30 04:35	3.2
Offset2_1 (KS 1741−293)	100027040	-0.416	-0.087	2005-09-24 13:44	1.9
Offset2_2 (KS 1741−293)	100037030	-0.416	-0.087	2005-09-30 06:06	2.9
Offset3_1 (1E 1743.1−2843)	100027050	0.251	-0.026	2005-09-25 18:00	1.9
Offset3_2 (1E 1743.1−2843)	100037050	0.251	-0.026	2005-10-01 06:57	2.3

*FOV center position.
†Effective exposure of the PIN data.
‡The positions of targeted point sources.
§Effective exposure of the XIS data.
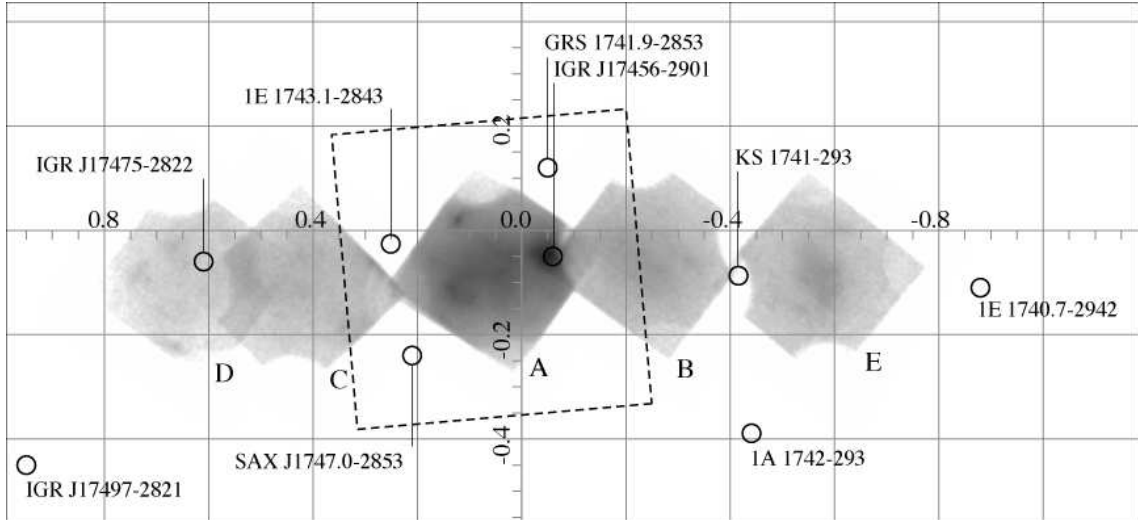
Fig. 1. A $2 - 10$ keV background-inclusive mosaic image of the Galactic center region taken with the XIS. The image is corrected for neither the exposure nor vignetting. The overlaid dotted square is the FWHM FOV of the PIN detector during the Region A observation. Black circles indicate the catalogued bright point sources that can contaminate the PIN signals (§4.4).
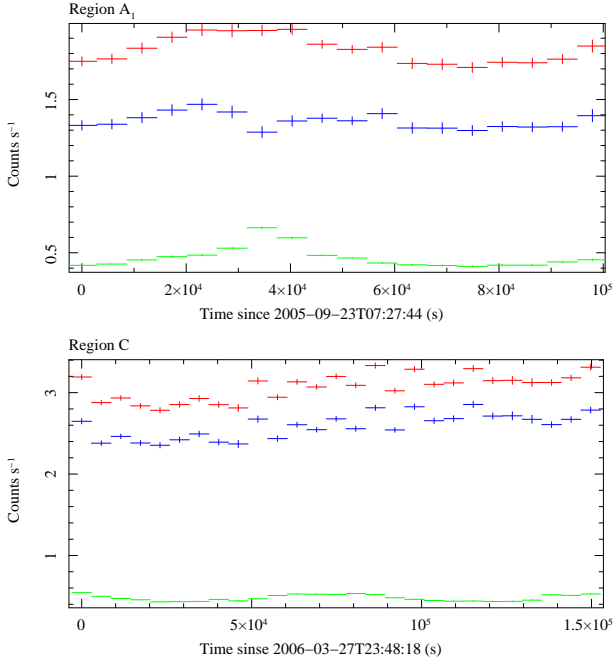
Fig. 2. HXD-PIN light curves of Region A_1 and Region C in the $10-40$ keV band, binned into 5760 s. Each plot shows raw counts (red), the modeled NXB (green), and the NXB-subtracted signals (blue).

shown in figure 2 (bottom), the count rate from Region C increased by $\sim 15\%$ in $\sim 1.5 \times 10^5$ s, presumably because a point source SAX J171747.0$-$2853, located outside the XIS FOV but inside the PIN FOV, varied during the present observation (§5.3).

4.2. Spectra

Figure 3 shows a typical example of the wide-band GC spectra, obtained from Region A_1 with XIS0 ($2-10$ keV) and 64 PIN diodes ($10-40$ keV). We limit the present analysis of the XIS data to energies above 2 keV, to avoid the contribution from a softer thermal component (Koyama et al. 2007a). The NXB subtracted HXD signal is so significant that it exceeds the NXB over $\sim 10-30$ keV band. Because the reproducibility of the PIN NXB is $3-5\%$ (Kokubun et al. 2007), we can claim the detection of a significant hard X-ray flux, at least up to ~ 40 keV in this particular case. For detailed analysis of the XIS data of these regions, Koyama et al. (2007a) may be referred to.

Region A was observed three times, with a time separation of a week between the first two observations, while a year till the last one. The NXB subtracted spectra of those three observations are shown in the bottom panel of figure 3. The data from the third pointing are corrected for the 25% loss of the PIN effective area (§3). The three spectra turned out to be very similar, with the $10-40$ keV PIN count rate (after the background subtraction) in agreement within $\sim 10\%$. Therefore, across the three observations, the hard X-ray emission from this region exhibited only minor variations, if any.

In the same panel, a model spectrum predicted for a 5 mCrab point source (a single power law of photon index $\Gamma = 2.1$) lo-

cated at the FOV center is also plotted. The observed PIN signals much exceed what is expected when a single point source, which roughly matches the XIS counts, was present at the FOV center of the XIS and PIN. We can explain this flux discrepancy in two alternative ways. One is to assume that the emission is extended, and hence HXD-PIN, which has a wider FOV than the XIS, received higher counts than the XIS. The other is to consider that bright point sources, which reside outside the XIS FOV but inside the PIN FOV, were contributing to the PIN flux.

In order to evaluate the above two alternatives, we present in figure 4 the background-subtracted wide-band spectra from all regions. We fitted these PIN spectra with a single power-law model. Although the emission may well be extended, we employed the response file for a point source located at the PIN optical axis. This is to make it easier to compare the detected flux with that of known bright point sources, which can contaminate the PIN signals (see below). The derived best fit parameters are listed in table 2. Among the 5 regions, except in Region C and D, the PIN signals have very similar intensities, as well as comparable spectral slopes. Even though there should be some point sources outside the XIS FOV but inside the HXD FOV, it would be rather difficult for them to be arranged in such a way that they contribute almost equally to Region A, B and E. Furthermore, in the $10-20$ keV band, the PIN signals exceed the point source model (figure 3 bottom) by a factor of $\sim 5-7$. The effective solid angle of the XIS and PIN are 168 and 1220 arcmin^2 respectively, and the factor is close to the solid angle difference between the two as $1220/168 = 7.3$. We therefore presume that a significant fraction of the PIN signals comes from celestial sources which are extended to the same order as the HXD-PIN FOV.

In table 2, some fits are not fully acceptable, and in such cases, the data are often found to be somewhat more convex than the model. Therefore, we fitted the PIN spectra also with a cutoff power-law model,

$$f(E) = K(E/1 \text{ keV})^{-\Gamma} \exp(-E/E_c), \qquad (1)$$

where E is the energy, $f(E)$ is the photon flux per unit energy interval, K is a normalization factor in units of photons keV^{-1} cm^{-2} s^{-1}, Γ is again the photon index, and E_c represents a typical energy scale of the spectral cutoff. The fit result improved slightly with reduced chi-squared of $0.75-1.5$, and the derived photon index and cutoff energy varied from region to region, over $1.2-2.2$ and $19-50$ keV, respectively.

4.3. Bright point sources

In the three offset observations, we clearly detected three bright point sources. As listed in table 1, they have been identified with catalogued sources, namely 1A 1742$-$294, KS 1741$-$293 and 1E 1743.1$-$2843, which are well known through previous observations. During the present pointings for a few ks each, these sources exhibited only mild variations up to 20%.

In the following analysis, we need to estimate the contribution of these point sources to the PIN signals detected from Region A through E, because the HXD has no imaging capability. Our strategy is to quantify their spectra in the XIS energy band ($2-10$ keV), and extrapolate the results to the PIN band ($12-40$ keV). The PIN data obtained in the offset
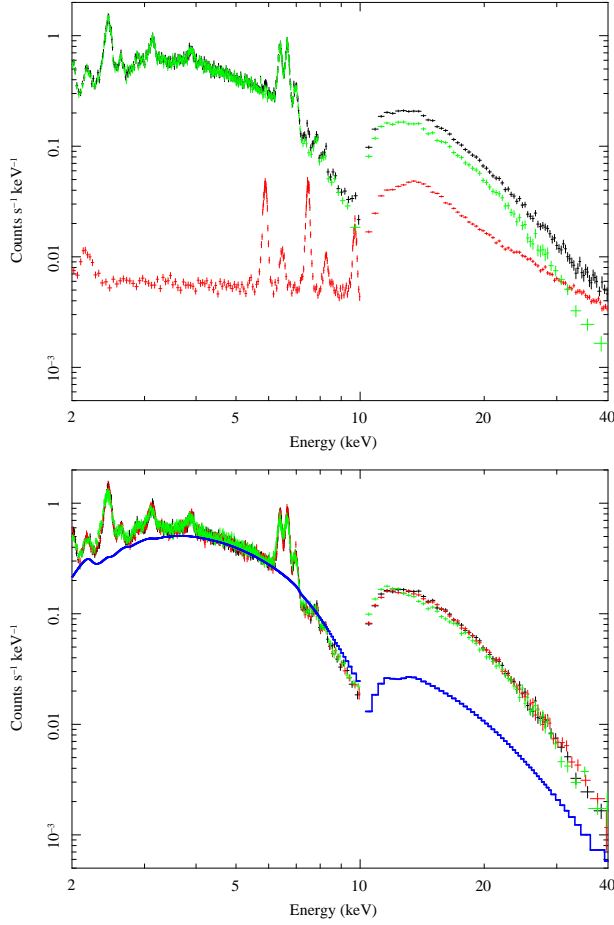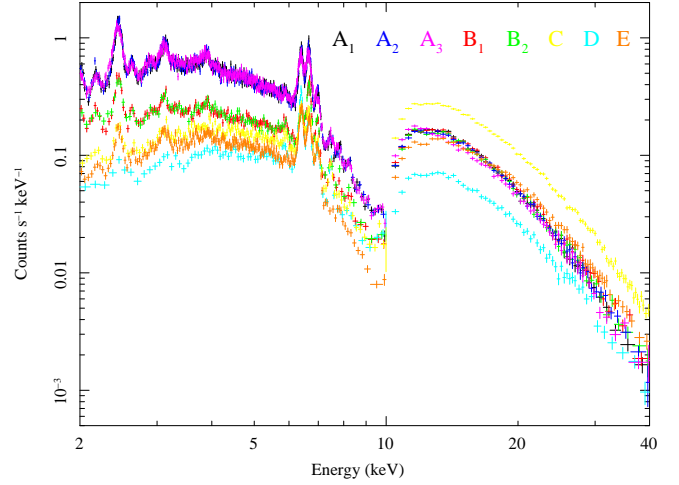
Fig. 4. Wide-band spectra of the 5 regions. Data obtained with XIS0 $(2 - 10$ keV) and HXD-PIN $(10 - 40$ keV) are plotted in the same manner as figure 3. Different observations are indicated by different colors, as specified in the figure.

Fig. 3. Top : Wide-band spectra of Region A_1, taken with XIS0 and PIN. Raw (black), NXB (red), and NXB-subtracted (green) spectra are plotted. Bottom : The NXB-subtracted spectra of XIS0 and PIN obtained in the first, second, and third observations of Region A, shown in black, red, and green crosses, respectively. The PIN spectrum of the third observation is scaled to 4/3 of the original one (see text). Blue solid line is a model spectrum of a 5 mCrab point source which has a single power-law spectrum with $\Gamma = 2.1$, absorbed by a hydrogen column of $N_H = 6 \times 10^{22}$ cm^{-2}.

Table 2. Results of the fitting to the PIN spectra from the 5 regions with a single power-law model.

Name	Photon Index[*]	Flux[†]	χ^2_ν[‡]
Region A_1	2.79 ± 0.04	2.86	0.98
Region A_2	2.68 ± 0.04	2.88	0.77
Region A_3	2.65 ± 0.04	2.66	1.42
Region B_1	2.62 ± 0.04	3.06	1.17
Region B_2	2.66 ± 0.04	2.89	1.39
Region C	2.20 ± 0.02	6.28	1.69
Region D	2.30 ± 0.05	1.53	1.02
Region E	2.08 ± 0.04	3.35	1.41

[*] Errors are at 90% confidence level.
[†] $12 - 40$ keV flux in units of 10^{-10} ergs cm^{-2} s^{-1}.
[‡] With 72 degrees of freedom.

observations were not used because they are contaminated by other bright point sources and possibly by the Galactic center extended emission itself. In order to minimize systematic errors in this process, we also refer to the literature on their spectra, obtained through past observations with various satellites. In particular, we use the INTEGRAL light curves of the GC region (Kuulkers et al. 2007), which is extracted using OSA6 software and distributed by the INTEGRAL Science Data Center (Courvoisier et al. 2003), to examine our spectral models for their consistency in the higher energy band $(20 - 60$ keV). To reduce statistical errors, we averaged INTEGRAL IBIS count rate of each point source over one week around our each observation. The used spectral model and the best fit parameters obtained in this way are listed in table 3, together with 90% confidence errors. Below, we briefly describe results on the three sources.

1A 1742−294 is a persistent low-mass X-ray binary (LMXB), and is known to harbor a neutron star, since recursive type-I X-ray bursts have been observed (e.g., Lewin et al. 1976; Sidoli et al. 1999; Sakano et al. 2002). Sidoli et al. (1999) reported that an absorbed single power-law model with $\Gamma \sim 1.7 - 1.9$, or an absorbed thermal bremsstrahlung model with a temperature of $kT \sim 10 - 16$ keV, gave an equally acceptable fits to the $2 - 10$ keV spectrum taken with the BeppoSAX MECS. Analyzing the XIS data, we obtained similar result with somewhat softer spectral parameters; a power law with $\Gamma \sim 2.0 - 2.2$, or a bremsstrahlung with $kT \sim 8.0 - 9.4$ keV. The achieved fit result is presented in figure 5. When extrapolated to higher energies, our bremsstrahlung model derived from the XIS data predicts an intensity of $5.9 - 7.8$ mCrab[1] in the $20 - 60$ keV INTEGRAL IBIS band. This is in a good agreement with the INTEGRAL measurement (Kuulkers et al. 2007), that the $20 - 60$ keV intensity of this source in the period of our observation was $\sim 5 \pm 1$ mCrab. In contrast, the power-law model determined by the XIS data predicts a hard X-ray

---

[1]   In the $20 - 60$ keV band, a 1 mCrab point source emits a flux of 1.38×10^{-11} ergs cm^{-2} s^{-1}.

intensity which is higher by a factor of $6 - 7$. We therefore regard the bremsstrahlung model as appropriate for the present purpose.

KS $1741-293$ is a transient LMXB with type-I X-ray bursts (in't Zand et al. 1991). Its spectrum was so far described with an absorbed single power-law model or an absorbed bremsstrahlung model (Sidoli et al. 1999; in't Zand et al. 1991), both yielding a relatively high hydrogen column density of $N_{\rm H} \sim 10^{23} {\rm cm}^{-2}$. Applying these two models to the XIS data, we obtained a close value as $N_{\rm H} \sim (1.6 - 2.1) \times 10^{23} {\rm cm}^{-2}$. The photon index ($\Gamma \sim 2.0 - 2.3$) of the power-law model and the temperature ($kT \sim 7.7 - 10$ keV) of the bremsstrahlung model, which we derived with the XIS, are not much different from the previous values of $\Gamma \sim 2.0 - 2.1$ of Sidoli et al. (1999) and $kT \sim 9$ keV of in't Zand et al. (1991), respectively. However, our bremsstrahlung modeling predicts a $20 - 60$ keV intensity of 0.7 mCrab, which is much lower than that measured with the INTEGRAL IBIS ($\sim 7 \pm 1$ mCrab). Therefore, when estimating the contribution of this source to the GC observations (see next subsection), we instead use our power-law modeling, which predicts a $20 - 60$ keV intensity of 4.4 mCrab and 2.6 mCrab for the first and second observations, respectively.

1E $1743.1-2843$ is a persistent X-ray source, but the type of its compact object is unknown because no type-I X-ray burst has been detected so far (e.g., Porquet et al. 2003; Cremonesi et al. 1999). BeppoSAX and ASCA observations showed that its spectrum can be better described by an absorbed blackbody model than by an absorbed power-law model or an absorbed bremsstrahlung (Cremonesi et al. 1999). In fact, the XIS spectrum was reproduced successfully by a black body model with a temperature of $kT = 1.8$ keV, absorbed by $N_{\rm H} = 13 \times 10^{22}$ cm^{-2}. However, according to Del Santo et al. (2006), wide-band spectra of this source, taken simultaneously with XMM-Newton, Chandra, and INTEGRAL IBIS, require a steep power-law component with $\Gamma \sim 3.1 - 3.3$ to be added to a blackbody model of $kT \sim 1.6 - 1.8$ keV, suggesting that the object may be a black-hole binary. Since our purpose is to extrapolate the spectrum from the XIS band to that of PIN, the hard tail component should not be neglected. Therefore, we also applied a black body plus power law model to the XIS data, in which the $20 - 100$ keV flux of the power-law component is fixed at 8×10^{-12} erg s^{-1} cm^{-2} but its slope is allowed to vary. This constraint on the flux was derived by scaling the $20 - 100$ keV flux of 1.7×10^{-11} erg s^{-1} cm^{-2} measured by Del Santo et al. (2006), to the flux ratio in the $2 - 10$ keV band, ~ 0.45, between their and our measurements. We have then obtained $kT = 1.8 - 1.9$ keV and $\Gamma = 2.9 - 3.2$, in a good agreement with Del Santo et al. (2006).

4.4.   Subtraction of bright point source contributions from the PIN spectra

As can be expected from figure 1, the PIN signals obtained in the present observations should be mixtures of the extended emission around the GC and the emission from known bright point sources. Therefore, to derive the surface brightness and net spectra of the extended emission, we need to estimate the contribution of those point sources and subtract it from the PIN spectra. For this purpose, we selected catalogued point sources
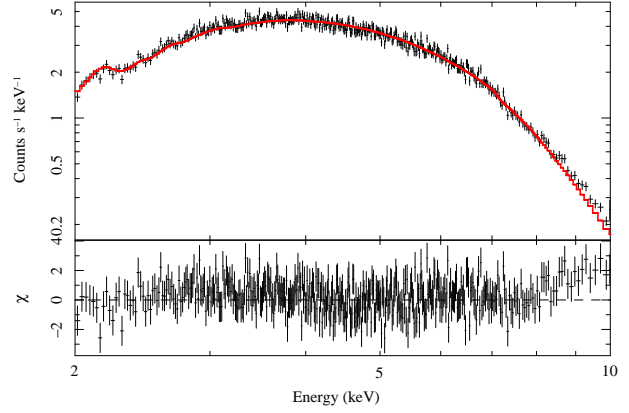

Fig. 5. The NXB-subtracted spectrum of Offset1_1 (1A $1742-294$) taken with XIS FI CCDs (black crosses), compared with the best fit bremsstrahlung model (red line).
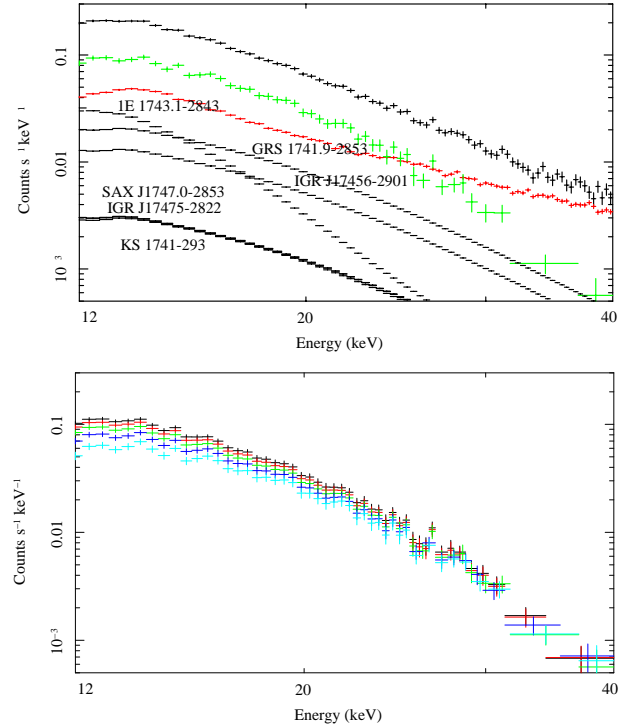

Fig. 6. Top : Raw PIN spectrum of Region A_1 (black), compared with the modeled NXB spectrum (red). Black lines show contributions from the bright point sources, estimated from the XIS offset observations for 1A $1742-294$, KS $1741-293$, and 1E $1743.1-2843$, or assuming power-law models of a photon index $\Gamma_{\rm p} = 2.1$ (for the "other" point sources). The residual spectrum, derived after subtracting the NXB and the point-source contributions, is plotted by green crosses. Bottom : The same data as the green data points in the top panel, but presented for four different point source estimations. Red, green, blue, and cyanic crosses represent the residual spectra obtained by changing $\Gamma_{\rm p}$ of the "other" point sources in the top panel to 1.5, 1.8, 2.1, 2.4 and 2.7, respectively.

Table 3. Spectral parameters of the three point sources determined with the XIS offset observations.[*]

Name	Model[†]	Column Density $(10^{22}\mathrm{cm}^{-2})$	Parameters kT(keV)	Γ	Flux[‡]	χ^2_ν
Offset1_1 (1A 1742−294)	TB	$6.0^{+0.1}_{-0.1}$	$8.0^{+0.3}_{-0.3}$		6.30	1.05 (1792)
	PL	$7.1^{+0.1}_{-0.1}$		$2.15^{+0.03}_{-0.03}$	6.35	1.02 (1792)
Offset1_2 (1A 1742−294)	TB	$5.7^{+0.1}_{-0.1}$	$9.4^{+0.4}_{-0.3}$		5.64	1.13 (1915)
	PL	$6.7^{+0.1}_{-0.1}$		$2.03^{+0.03}_{-0.03}$	5.67	1.10 (1915)
Offset2_1 (KS 1741−293)	TB	$18.9^{+1.1}_{-1.1}$	$7.6^{+1.4}_{-1.1}$		0.52	0.95 (319)
	PL	$20.9^{+1.5}_{-1.4}$		$2.3^{+0.1}_{-0.1}$	0.52	0.97 (319)
Offset2_2 (KS 1741−293)	TB	$16.0^{+1.3}_{-1.2}$	$10.1^{+3.8}_{-2.1}$		0.23	0.92 (240)
	PL	$17.6^{+1.7}_{-1.6}$		$2.0^{+0.2}_{-0.2}$	0.23	0.92 (240)
Offset3_1 (1E 1743.1−2843)	BB	$10.8^{+0.7}_{-0.7}$	$1.8^{+0.1}_{-0.1}$		1.03	1.00 (487)
	BB+PL	$15.0^{+2.4}_{-3.4}$	$1.9^{+0.1}_{-0.1}$	$3.0^{+0.3}_{-0.7}$	1.04	0.99 (486)
Offset3_2 (1E 1743.1−2843)	BB	$12.2^{+0.6}_{-0.6}$	$1.9^{+0.1}_{-0.1}$		1.60	1.10 (773)
	BB+PL	$17.4^{+2.4}_{-2.7}$	$2.0^{+0.1}_{-0.1}$	$3.2^{+0.2}_{-0.4}$	1.60	1.09 (772)

[*]Errors are at 90% confidence level.
[†]TB:thermal bremsstrahlung (`bremss` in XSPEC), PL:power law (`powerlaw`), BB:black body (`bbdoy`), BB+PL:black body
plus power law with pegged flux 8×10^{-12}ergs cm^{-2} s^{-1} in $20-100$ keV.
[‡]Unabsorbed flux ($2-10$ keV) in units of 10^{-10} ergs cm^{-2} s^{-1}

Table 4. The list of bright ($\gtrsim$1 mCrab in the $12-40$ keV band) point sources that can exist inside the PIN FOV in the observations of Region A−E.

Name	l (°)	b (°)	Rate (cts s^{-1})[*] 1st	2nd
1E 1740.7−2942	-0.88	-0.11	10.2	10.4
1A 1742−294[†]	-0.44	-0.39	1.2	1.3
KS 1741−293[‡]	-0.43	-0.09	1.9	1.7
IGR J17456−2901	-0.06	-0.05	0.7	0.7
GRS 1741.9−2853	-0.05	0.12	1.3	0.5
SAX J1747.0−2853	0.21	-0.24	0.2	0.2
1E 1743.1−2843[§]	0.26	-0.03	1.2	1.0
IGR J17475−2822	0.61	-0.06	0.8	0.8
IGR J17497−2821	0.95	-0.45	1.0	0.9

[*]A week averaged INTEGRAL IBIS count rate ($20-60$ keV) in the first and second observation of Region A and B with a typical error of ± 0.3 cts s^{-1}. 5 cts s^{-1} corresponds to $\sim$20 mCrab (2.8×10^{-10} ergs cm^{-2} s^{-1}) in the $20-60$ keV band.
[†]Offset1 [‡]Offset2 [§]Offset3

that can be brighter than 1 mCrab in our observations, and located in the $l < |1°.5|$ and $b < |1°|$ region because the full FOV of PIN is $\sim 1° \times 1°$. At the 8 kpc distance, the threshold of 1 mCrab corresponds approximately to a $2-40$ keV luminosity of $\sim 3.5 \times 10^{35}$ erg s^{-1}. Table 4 shows a list of the selected sources ordered by their Galactic longitudes. Although the PIN signals must be contributed also by more numerous uncatalogued (and mostly dimmer) point sources, we include them into what we call "extended" emission, because, in hard X-ray band, their contribution cannot be estimated at present with a sufficient reliability.

Here, we limit our detailed analysis to the first and second observations of Region A and B, namely A$_1$, A$_2$, B$_1$, and B$_2$, because the XIS offset observations of the three point sources were conducted within a few days of these four point-

ings, and hence their contributions can be most accurately estimated. Specifically, we estimated the $12-40$ keV spectra of the three objects, by extrapolating the best fit model obtained in §4.3; a bremsstrahlung with $kT = 7.98$ and 9.37 keV for 1A 1742−294, a power law with $\Gamma = 2.26$ and 2.04 for KS 1741−293, and a blackbody ($kT = 1.85, 1.98$ keV) plus power law ($\Gamma = 2.95, 3.21$) for 1E 1743.1−2843. Each parameter is assigned a pair of values, applicable in this order to the first and second observations of those objects. The estimated spectra were then multiplied by the angular response of HXD-PIN (figure 8 of Takahashi et al. 2007), considering angular offsets of these objects (from the PIN optical axis) in each pointing observation. The relative normalization difference by $\sim 13\%$, between the XIS and PIN (Kokubun et al. 2007), was also considered by multiplying 1.13 to the normalization parameter derived from the XIS spectra.

Besides the three sources, there are 6 catalogued point sources, as listed in table 4, which can contribute to the PIN signals. Since we do not have direct XIS information on them, we assumed all of them to have power-law spectra with a common photon index Γ_p, and adjusted individual normalizations so that their week-averaged $20-60$ keV intensities, as recorded by INTEGRAL IBIS (§4.3), can be reproduced. Their spectra estimated in this way were then multiplied by the HXD-PIN angular response, in the same way as for the preceding three sources.

Figure 6 (top panel) exemplifies the estimated spectra of the listed point sources, and the residual PIN spectra (green) obtained after subtracting the NXB and all these point source contributions. Since the current PIN response below 12 keV contains rather large uncertainty, the point source simulation was conducted in the $12-40$ keV band. The bottom panel of figure 6 illustrates how the residual PIN spectrum changes as the common photon index assumed for the point sources (other than the three) is varied as $\Gamma_\mathrm{p} = 1.5, 1.8, 2.1, 2.4$ and 2.7. Thus, the residual PIN signal is highly significant, even Γ_p is

changed over a plausible range. The difference of the residual flux between the two extreme cases, $\Gamma_p = 1.5$ and 2.7, is ~ 2.

We analyzed the data from Region A_2, B_1, and B_2 in the same manner as Region A_1. The obtained residual PIN spectra are shown in figure 7, where contributions of the three point sources were treated individually, while those of the other listed sources were modeled with $\Gamma_p = 2.1$ and adjusted as described before. Thus, the residual signals from Region A_2, B_1 and B_2 are also significant. Furthermore, the signals from Region A and Region B are very similar both in the normalization and the spectral slope, even after removing the estimated contributions from the known point sources.

As mentioned in §4.2, the ratio between the XIS and PIN signals are different from what is expected from a point source. We roughly explained the PIN signal excess over a predicted point source spectrum, based on its larger effective solid angle than that of the XIS, and the uniform spatial extent of the emission. Then, we subtracted the bright point source contribution, and found the PIN signals to be roughly halved in each region. Nevertheless, these residual PIN spectra still exceed significantly the model spectrum for a 5 mCrab point source (blue solid line in figure 3 bottom), reconfirming the extended nature of the emission as noted in §4.2. We further consider the surface brightness distribution of the extended emission in §4.6.

4.5. Fitting to the HXD spectra

Assuming that the emission uniformly fills the HXD-PIN FOV, we fitted the residual PIN spectra (figure 7) with several simple models; a thermal bremsstrahlung, a power law, a broken power law, and a cutoff power law of equation (1). A broken power-law model is expressed as

$$f(E) = \begin{cases} K(E/1\,\mathrm{keV})^{-\Gamma_1}, & E < E_c \\ KE_c^{\Gamma_2 - \Gamma_1}(E/1\,\mathrm{keV})^{-\Gamma_2}, & E > E_c, \end{cases} \quad (2)$$

where K is a normalization factor similar to that in equation (1), and E_c is an energy of a spectral break point. The photon indices below and above E_c are denoted as Γ_1 and Γ_2, respectively. To avoid the uncertainty included in the PIN response below 12 keV, we limited the PIN spectral fitting to the $12 - 40$ keV band. The model spectrum contains the small contribution of the cosmic X-ray background, which is typically ~ 5 % of the NXB. Results of these fits are summarized in table 5, together with the $12 - 40$ keV surface brightness implied by the model.

Table 5 indicates that the residual spectrum of Region A (both A_1 and A_2) prefer convex models (thermal bremsstrahlung, broken power law, and cutoff power law) to the straight power-law model. Indeed, as shown in figure 8, a power-law fit to the Region A_1 spectrum leaves significant fit residuals in the < 15 keV and > 30 keV regions, while a cutoff power-law model is fully acceptable. This is the same tendency as already noticed at the end of §4.2 before subtracting the point source contributions. Spectra of Region B exhibit a similar preference, though less significant. If, e.g., the thermal bremsstrahlung fits are employed, the spectra from all these regions are characterized by a very high temperature of ~ 15 keV. The cutoff power-law fits lead to similar cutoff "temperature". If, instead, the broken power-law modeling is adopted, the four spectra are
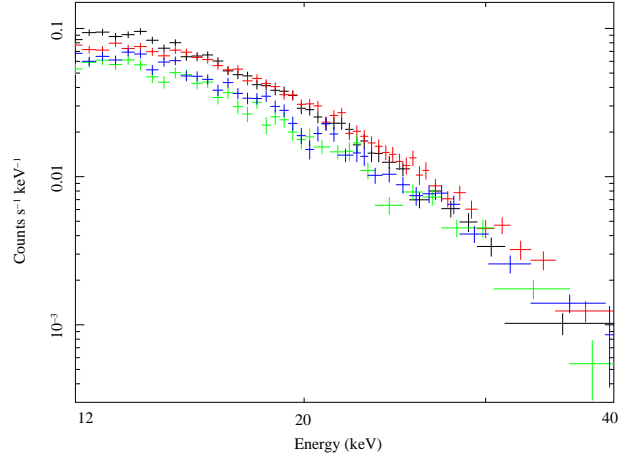

Fig. 7. The residual PIN spectra of Region A_1 (black), A_2 (red), B_1 (green), and B_2 (blue). Contributions from 1A 1742−294, KS 1741−293 and 1E 1743.1−2843 were estimated and subtracted individually (see text), while those from the other catalogued point sources were removed assuming $\Gamma_p = 2.1$.

consistently represented by a photon index of $\Gamma_1 \sim 2$ and $\Gamma_2 \sim 3$ in energies below and above ~ 20 keV, respectively.

We examined how the fit results are affected by the value of Γ_p assumed for the "other" point sources. As a representative case, the bottom half of table 5 gives the best fit parameters of Region A_1, obtained by changing Γ_p from 2.1 to 1.8, or to 2.4. Since the $20 - 60$ keV fluxes of the "other" point sources are individually fixed using the INTEGRAL data, a harder (smaller) value of Γ_p makes the residual PIN spectrum softer. Nevertheless, the implied $12 - 40$ keV surface brightness does not differ by more than ~ 20% between the cases with $\Gamma_p = 1.8$ and $\Gamma_p = 2.4$.

4.6. Simultaneous fitting to the XIS and PIN spectra

Analyzing the XIS data of the extended GC emission, Koyama et al. (2007a) reported the presence of a power-law-like hard tail with a photon index of $1.4^{+0.5}_{-0.7}$, in addition to the line-rich hot (~ 6.5 keV) thermal emission. However, in the XIS range, these two components have relatively similar spectral slopes. Therefore, to more accurately distinguish them, it is important to expand the available energy range by combining the XIS and HXD results.

The residual PIN spectra of Region A and B, obtained in the previous subsection by excluding the contribution from the catalogued bright point sources, have a $10 - 15$ keV slope of ~ 1.5, in terms of a broken power-law modeling. Since this is close to that of the XIS hard tail found by Koyama et al. (2007a), the residual PIN spectra are considered to reflect mainly the extended GC emission (its hard tail component in particular) that is also observed by the XIS. Therefore, we tried a simultaneous fit to the XIS and PIN data. Hereafter, we set $\Gamma_p = 2.1$ to subtract the contributions of the "other" point sources from the PIN signals.

One obvious problem in the XIS plus HXD simultaneous fitting is that the HXD, with a larger FOV, receives the extended signals even from outside the XIS FOV. However, according to Koyama et al. (2007a) and Nobukawa et al. (2007), the

Table 5. Results of model fits to the residual PIN spectra.[*]

Region	Model[†]	Parameters				Σ[§]	χ^2_ν (ν)
		kT (keV)	Γ_1	Γ_2	E_c[‡] (keV)		
A1	TB	$12.8^{+0.8}_{-0.7}$				4.70	0.86 (72)
	BKNPL		$2.5^{+0.0.2}_{-0.2}$	$4.1^{+1.6}_{-0.6}$	$21.9^{+4.3}_{-3.1}$	4.63	0.87 (70)
	CUTOFFPL		$0.9^{+0.5}_{-0.7}$		$9.3^{+2.9}_{-2.5}$	4.65	0.83 (71)
	PL		$2.8^{+0.1}_{-0.1}$			4.85	1.38 (72)
B1	TB	$16.3^{+1.9}_{-1.6}$				3.28	1.20 (72)
	BKNPL		$2.5^{+0.1}_{-0.1}$	$27.0^{+0.1}_{-23}$	$36.7^{+2.0}_{-7.7}$	3.30	1.13 (70)
	CUTOFFPL		$2.0^{+0.5}_{-0.7}$		$35.4^{+164}_{-35.3}$	3.33	1.18 (71)
	PL		$2.6^{+0.1}_{-0.1}$			3.35	1.18 (72)
B2	TB	$17.4^{+1.7}_{-1.5}$				3.78	1.33 (72)
	BKNPL		$1.6^{+2.9}_{-2.4}$	$2.6^{+0.1}_{-0.1}$	$14.0^{+4.8}_{-1.2}$	3.83	1.30 (70)
	CUTOFFPL		$1.8^{+0.7}_{-0.6}$		$27.1^{+172.9}_{-12.4}$	3.80	1.33 (71)
	PL		$2.5^{+0.1}_{-0.1}$			3.88	1.35 (72)
A2	TB	$21.9^{+1.8}_{-1.6}$				5.20	0.85 (72)
	BKNPL		$1.3^{+0.4}_{-0.9}$	$2.7^{+0.2}_{-0.2}$	$16.6^{+2.0}_{-1.9}$	5.15	0.67 (70)
	CUTOFFPL		$0.3^{+0.4}_{-0.6}$		$10.1^{+3.1}_{-2.5}$	5.10	0.69 (71)
	PL		$2.3^{+0.1}_{-0.1}$			5.30	1.35 (72)
A$_1$ ($\Gamma_p = 1.8$)[‖]	TB	$12.2^{+0.7}_{-0.6}$				5.08	0.87 (72)
	BKNPL		$2.6^{+0.1}_{-0.2}$	$4.2^{+1.4}_{-0.6}$	$22.0^{+3.8}_{-2.8}$	5.00	0.88 (70)
	CUTOFFPL		$0.9^{+0.5}_{-0.7}$		$9.0^{+2.7}_{-2.3}$	5.03	0.84 (71)
	PL		$2.9^{+0.1}_{-0.1}$			5.25	1.50 (72)
A$_1$ ($\Gamma_p = 2.4$)[‖]	TB	$14.1^{+1.0}_{-1.0}$				4.30	0.86 (72)
	BKNPL		$2.4^{+0.2}_{-0.2}$	$3.9^{+1.7}_{-0.6}$	$21.7^{+4.9}_{-3.4}$	4.23	0.86 (70)
	CUTOFFPL		$0.8^{+0.5}_{-0.8}$		$9.4^{+3.6}_{-2.7}$	4.25	0.82 (71)
	PL		$2.7^{+0.1}_{-0.1}$			4.43	1.28 (72)

[*]Errors are at 90% confidence level.
[†]TB : thermal bremsstrahlung (`bremss` in XSPEC). BKNPL : broken power law (`bknpower`). CUTPL : cutoff power law (`cutoffpl`). PL : power law (`powerlaw`).
[‡]The cutoff energy in the cutoff power-law model or the energy for the broken point in the broken power-law model.
[§]$12 - 40$ keV surface brightness in units of 10^{-10} ergs cm^{-2} s^{-1} deg^{-2}
[‖]Results obtained by changing the photon index Γ_p for "other" point sources to 1.8 or 2.4.

[Fe XXVI Kα]/[Fe XXV Kα] line flux ratio of the GC extended emission in the $-0°4 < l < 0°6$ region is almost constant at ~ 0.4. Therefore, we can assume, at least in Region A, that the spectral shape is constant inside the PIN FOV, and only the surface brightness varies from place to place. Since the Fe line flux ratio has not yet been precisely measured in $l < -0°5$, and the PIN FOV during the Region B observation extends much into the $l < -0°5$ region, below we limit our analysis to the Region A data. Then, we combined the XIS and PIN spectra from the two observations (A$_1$ and A$_2$) and derived the averaged spectra, because the two observations gave very similar spectra (figure 3 and 4). To avoid contributions of the cooler ($\lesssim 1$ keV) thermal component, we limited the fit energy range of the XIS data to > 5.5 keV after Koyama et al. (2007a).

When using the XIS data from Region A, another particular caution is needed; we must exclude signals from the bright Sgr A East region (or the Sgr A* complex). According to Koyama et al. (2007c), the XIS spectrum of this region exhibits two thermal components, and a power-law hard tail with $\Gamma \sim 0.8$ which is estimated to contribute a flux of 5.2×10^{-11} ergs cm^{-2} s^{-1} to the $12 - 40$ keV PIN data (before applying the $65 - 75\%$ PIN angular transmission). We then excluded this region from the XIS event integration, by masking a circular region of radius $3'$ centered on $(l, b) = (+359°95, -0°050)$.

When we turn to the PIN data, in §4.4 we have subtracted the contribution from "point source" IGR J17456-2901, which is reported to coincide with Sgr A East region and Sgr A* (e.g., Neronov et al. 2005). During our observations of Region A and B, IGR J17456-2901 was reported to exhibit roughly a constant $20 - 60$ keV flux of $(4.1 \pm 1.7) \times 10^{-11}$ ergs cm^{-2} s^{-1} by INTEGRAL IBIS, which predicts the $12 - 40$ keV flux of $(4.8 \pm 2.0) \times 10^{-11}$ ergs cm^{-2} s^{-1} when extrapolated with $\Gamma = 2.1$. Since this value agrees well with that of the excluded XIS region, and the thermal component of the emission decreases rapidly becoming much less dominant than the power-law component in the PIN band, we conclude that the contribution from the Sgr A East region has been removed from both the XIS and HXD data in a consistent manner.

In the combined fitting, we used the following three models; (a) a collisional ionization equilibrium (CIE) plasma emission (`apec` version 1.3.1) plus three gaussian lines, (b) the same as (a) but a power law is added; and (c) the same as (b) but the
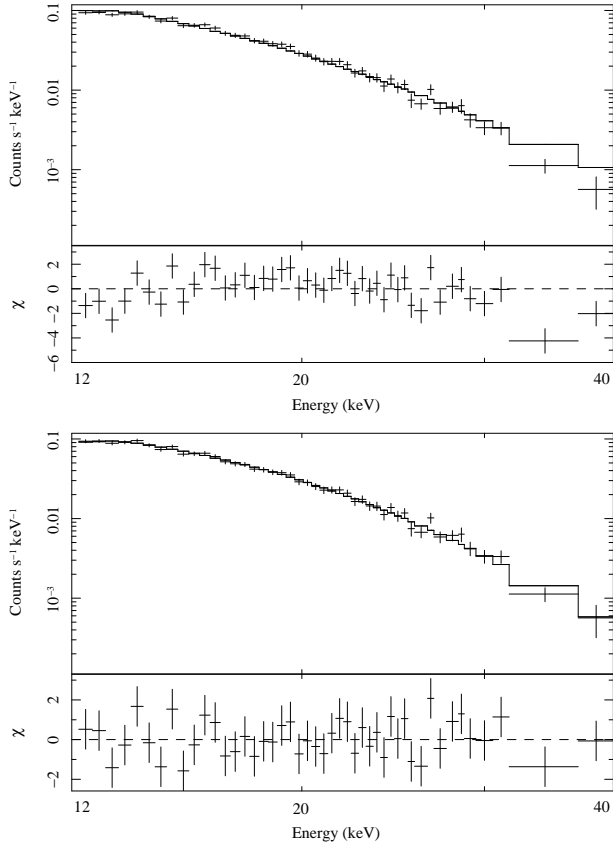
Fig. 8. The residual PIN spectrum of Region A_1 (black crosses in figure 7) fitted with a power-law model (top) and a cutoff power-law model (bottom).

power law is replaced by a cutoff power-law model. Among them, (b) is the same as in Koyama et al. (2007a). The three gaussians represent the neutral (or low ionizaed) Fe $K\alpha$, Fe $K\beta$, and Ni $K\alpha$ lines. In each model, we subjected all the model components to a common absorption fixed at 6×10^{22} cm^{-2}, and multiplied the PIN model with a constant (but free) factor; the latter is intended to compensate for the difference of the model normalization between the two instruments, caused by possible nonuniformity of the surface brightness: an implicit assumption is that the multiple spectral components comprising a model have similar surface brightness distributions within each PIN FOV. The iron abundance of the `apec` model was at first allowed to vary freely, but was not well constrained. Therefore we fixed it to 1.0 solar, and examined the result by changing it as 0.5 and 2.0 (see below). Additionally, we introduced a small red-shift to the XIS model spectrum, to compensate for the uncertainty of gain calibration as noted in Koyama et al. (2007a). The backside illuminated CCD chip (XIS1) is not utilized in the combined fit because it suffers from rather high NXB counts above $\sim 7-8$ keV. We assumed a circular emission region with a radius of $60'$ in calculating the XIS ancillary response file by `xissimarfgen`. With these assumptions, we expect the XIS versus PIN normalization ratio to become unity when the emission has a uniform brightness over the detector FOVs.

Figure 9 shows results of the simultaneous fitting to the XIS

and PIN spectra. Model (a) failed to reproduce the spectra with $\chi_\nu^2 = 3.32$ (740). The derived plasma temperature of $kT = 9.2$ keV is much higher than the value of $6.4 - 6.6$ keV calculated based on the Fe line intensity ratio (Koyama et al. 2007a). Moreover, the extrapolated thermal model falls significantly short of the observed PIN spectrum. All these results indicate that a separate hard tail component is necessary, thus reconfirming Koyama et al. (2007a).

Models (b) and (c) gave much more successful fits to the spectra, with χ_ν^2=1.52 (738) and χ_ν^2=1.01 (737), respectively. As listed in table 6, the plasma temperatures derived with these models are both consistent with the above quoted XIS measurement. However, Model (b) gives a photon index of $\Gamma = 1.86$ which is steeper than the XIS determination, and is over-predicting the counts in energies above ~ 25 keV. Model (c), with a photon index of $\Gamma = 0.47$ and a cutoff energy of $E_c = 9.9$ keV, better reproduce the XIS and PIN spectra. Therefore, the cutoff power-law modeling in Model (c) is considered more appropriate than the simple power law employed in Model (b), in agreement with the result obtained using the PIN spectra alone (§ 4.5).

With Models (b) and (c), the constant factor adjusting the model normalization to fit the PIN data was obtained as 0.46 and 0.34, respectively. This means that the extended emission is brighter inside the XIS FOV, because a largely extended emission with uniform brightness would make this factor 1.0.

We repeated the same analysis by changing the iron abundance as 0.5 and 2.0, to find that the essential properties of the results obtained assuming the 1.0 abundance remain unchanged. At the same time, we examined the uncertainty of 5% in the PIN NXB modeling, and confirmed the same results within the statistical errors. In addition, the results were qualitatively unchanged when we varied the modeling of the bright (3 plus 11) point sources within plausible tolerance (e.g., changing Γ_p of "the other" sources or replacing a power law to a cutoff power law). Therefore we conclude that the residual PIN spectra of Region A, combined with that from the XIS, require the hard tail other than a thermal component, and the hard tail exhibits a mildly convex shape in the higher energy band.

5. Discussion

5.1. Summary of the obtained results

In the HXD-PIN $10-40$ keV band, we detected intense hard X-ray signals from all the five regions around the GC. Except for one case, the PIN signal counts did not vary significantly within each observation (figure 2). When some regions were observed multiple times, neither the hard X-ray intensity nor the spectral shape changed significantly (figure 3, figure 4). The background-subtracted PIN spectra are approximated by a power-law model of $\Gamma = 2.0 - 2.7$, with a typical $12-40$ keV flux of $(3-4) \times 10^{-10}$ ergs cm^{-2} s^{-1} per PIN FOV (table 2).

In all cases, the background-subtracted PIN signals exceeded what would be expected from the XIS data of the same pointings (figure 3, figure 4), due most likely to the difference between their fields of view. Using the offset XIS observations (figure 5) and near-simulatateous INTEGRAL coverage, we subtracted contributions of catalogued bright point sources
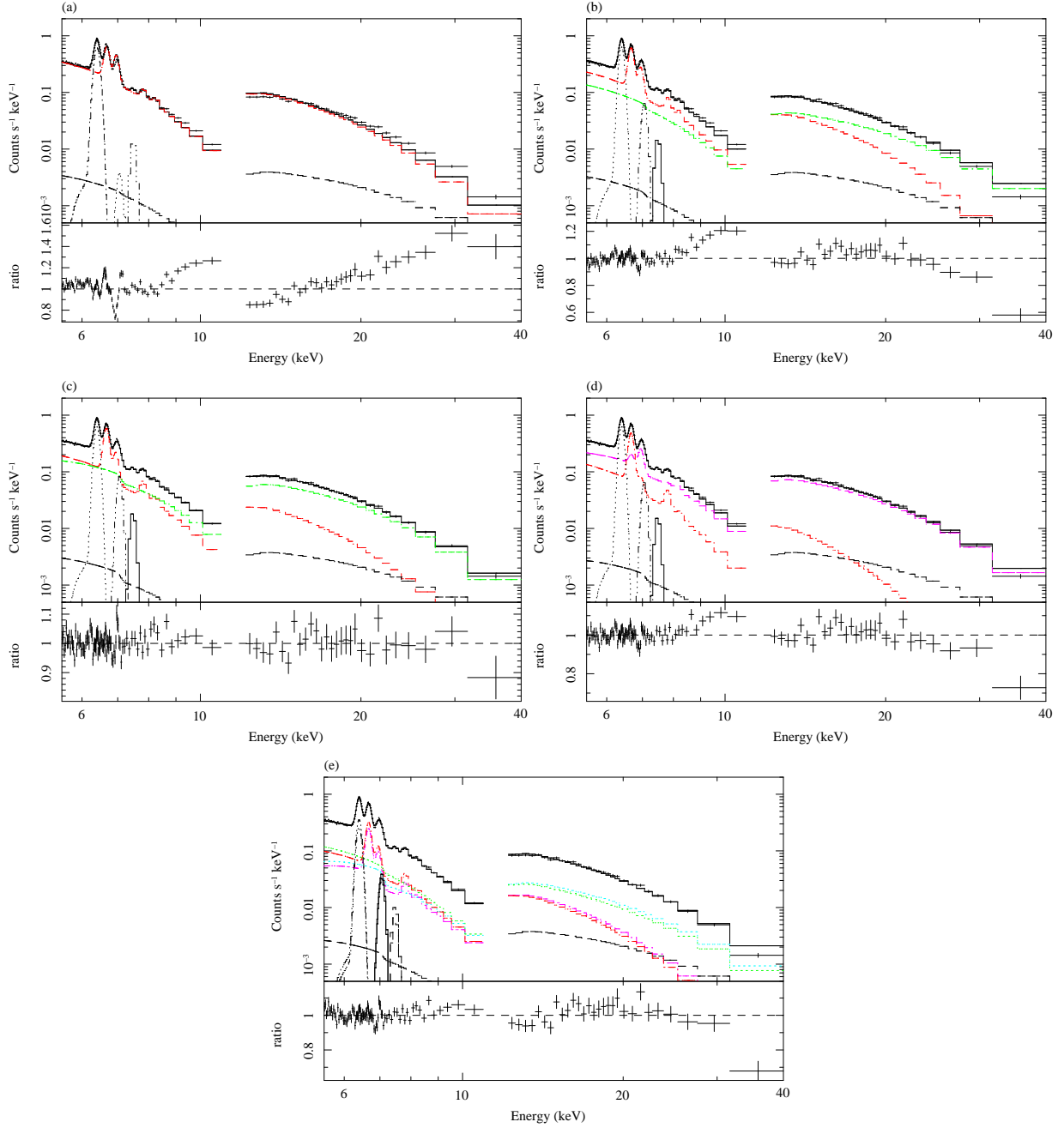
Fig. 9. The XIS and PIN spectra from Region A averaged over the first and second observations, simultaneously fitted by different models. The cosmic X-ray background is included as a fixed model, which is indicated by black dashed lines in each panel. The fit residuals are plotted in the bottom half of each panel as the data to model ratio. (a) A result with a CIE model and 3 gaussians. (b) A fit with a CIE model, 3 gaussians, and a power law. The contribution of the CIE plasma and the power-law tail are plotted by red and green dashed lines, respectively. (c) The same as panel (b) but the power law is replaced by a cutoff power law (also plotted by green dashed line). (d) A result with two CIE plasma model, plus 3 gaussians. The low and high temperature components are plotted by red and magenta dashed lines, respectively. (e) A fit with the partially covered model (see §5.5). The normally absorbed CIE model and power-law tail are plotted by red and green dashed lines, while highly absorbed components are indicated by magenta and cyanic dashed lines.

Table 6. Results of simultaneous fits to the XIS and residual PIN spectra of Region A.*

	(b)TH+PL[†]	(c)TH+CUTPL[†]
$N_{\rm H}$ (cm^{-2})	6×10^{22} (fixed)	6×10^{22} (fixed)
$N_{\rm Fe}$ (cm^{-2})	$6.2^{+0.6}_{-0.6} \times 10^{18}$	$10.9^{+1.2}_{-0.3} \times 10^{18}$
Therma		
kT (keV)	$7.0^{+0.1}_{-0.1}$	$6.2^{+0.1}_{-0.1}$
$Z_{\rm Fe}$ (solar)	1.0 (fixed)	1.0 (fixed)
$Z_{\rm Ni}$ (solar)	$2.1^{+0.3}_{-0.3}$	$2.2^{+0.3}_{-0.5}$
Redshift	$1.8^{+0.1}_{-0.1} \times 10^{-3}$	$1.9^{+1.1}_{-0.1} \times 10^{-3}$
Norm.[‡]	$3.63^{+0.03}_{-0.03}$	$3.55^{+0.04}_{-0.04}$
Emission lines		
Fe I[§] Kα		
$E_{\rm center}$ (eV)	6403^{+1}_{-1}	6401^{+1}_{-1}
σ (eV)	11^{+5}_{-11}	12^{+12}_{-8}
Intensity[‖]	$3.18^{+0.05}_{-0.05} \times 10^{-2}$	$3.26^{+0.01}_{-0.01} \times 10^{-2}$
Fe I[§] Kβ		
$E_{\rm center}$[#] (eV)	7062	7060
σ[#] (eV)	12	13
Intensity[‖]	$4.2^{+0.1}_{-0.1} \times 10^{-3}$	$5.6^{+0.3}_{-0.4} \times 10^{-3}$
Ni I[§] Kα		
$E_{\rm center}$ (eV)	7486^{+21}_{-21}	7478^{+20}_{-16}
σ (eV)	0 (fix)	0 (fix)
Intensity[‖]	$1.5^{+0.4}_{-0.4} \times 10^{-3}$	$2.1^{+0.3}_{-0.6} \times 10^{-3}$
Hard tail		
Γ	$1.86^{+0.01}_{-0.01}$	$0.47^{+0.01}_{-0.01}$
$E_{\rm c}$ (keV)	—	$9.9^{+0.1}_{-0.1}$
Norm.**	$8.21^{+0.15}_{-0.15} \times 10^{-1}$	$1.66^{+0.02}_{-0.03} \times 10^{-1}$
Constant	$0.45^{+0.01}_{-0.01}$	$0.34^{+0.06}_{-0.04}$
$\chi^2_\nu (\nu)$	1.51 (738)	1.01 (737)

*Errors are at 90% confidence level.

[†]TH+PL : a CIE plasma emission plus three gaussian lines with a power-law tail. TH+CUTPL : a CIE plasma emission plus three gaussian lines with a cutoff power-law tail.

[‡]$10^{-14}/(4\pi D^2) \int n_e n_H dV$, where D is the distance to the source (cm), n_e and n_H are the electron and hydrogen density in cm^{-3}, respectively.

[§]Or in low ionization states.

[‖]In units of photons s^{-1} cm^{-2}.

[#]Fixed at $1.103 \times E_{\rm center}$(Fe I K$\alpha$) and $1.103 \times \sigma$(Fe I Kα).

**In units of photons s^{-1} cm^{-2} keV^{-1} at 1 keV.

(table 4) that fall inside the PIN FOV. The PIN signals were then typically halved (figure 6), but still remained significant up to ~ 40 keV (figure 7). Therefore, we consider that the hard X-ray emission is also as extended as the thermal emission observed in < 10 keV. The derived residual PIN spectra exhibit mildly convex shapes (figure 8, table 5).

By fitting the XIS and PIN data of Region A simultaneously, we have shown that the broad-band (5-40 keV) spectrum of the extended X-ray emission cannot be reproduced by a single CIE model plus gaussian lines, but requires an additional harder component which was first suggested by Koyama et al. (2007a) (figure 9). This harder component is successfully reproduced by a mildly curving cutoff power-law model, while a single power law is less successful (table 6). As judged from the derived PIN vs. XIS normalization, the surface brightness of the hard emission is inferred to decrease toward the periphery of the PIN FOV, rather than being uniform within it.

5.2. Surface brightness distribution

To study a degree-scale surface brightness distribution of the extended GC emission in the PIN band, we further derived the residual PIN signals from Regions A$_3$, C, D, and E. In estimating and subtracting contributions from "the other" sources, the method described in §4.4 was used assuming $\Gamma_{\rm p} = 2.1$. Although near simultaneous XIS data on the three point sources are no longer available, we estimated their contributions assuming that their spectral shape did not change from the first offset XIS data acquired on 2005 September, and setting their normalization parameters to reproduce the one-week-averaged INTEGRAL IBIS flux obtained around the observation date of those regions.

The $12 - 40$ keV count rates of the residual PIN data, obtained in this way, are shown in figure 10 as a function of the galactic longitude. In all regions, the residual counts are thus positive. Furthermore, the emission detected with PIN is spatially more extended than a point source, as the measured longitude distribution is clearly wider than the PIN angular response for a point source (a red triangle).

Using the ASCA GIS data, Maeda (1998) have shown that the surface brightness of the 6.7 keV Fe line around the GC decreases along the longitudinal direction on two angular scales, $0°\!.42 \pm 0°\!.06$ and $\sim 15°$. To compare the present hard X-ray results with the Fe line intensity distribution, we modeled the latter as $\propto \exp[-(l+0°\!.05)/0°\!.42]$, and convolved it with the PIN angular response. The larger angular scale of Maeda (1998) can be neglected, and the offset of $l = -0°\!.05$ represents the peak structure of the line emission around Sgr A∗.

As presented in figure 10, the convolved Fe line intensity distribution has come to a close agreement with the longitudinal PIN count-rate profile. Even considering that the PIN signals are partially contributed by the thermal component to which the Fe lines are associated, the hard X-ray emission is inferred to have a similar spatial distribution as the hot thermal emission.

5.3. The case of Region C

As noted earlier, Region C exhibited almost twice higher counts in the PIN band than the other regions (figure 4), even though the XIS data of the region show no corresponding sign.
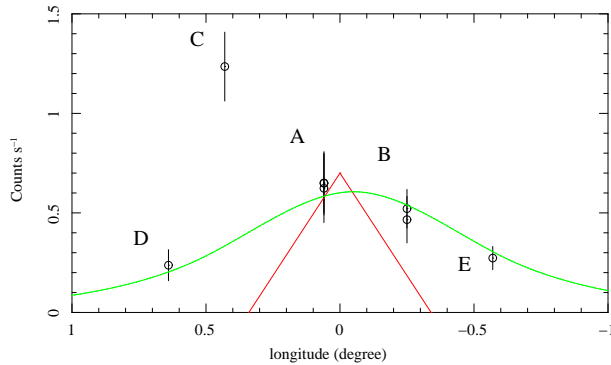
Fig. 10. The galactic longitude distributions of the apparently extended emission components. Black circles show the $12 - 40$ keV PIN count rates obtained after subtracting the NXB and the contributions from bright point sources. The error bars represent uncertainties of the estimation of fluxes of the bright point sources. The green curve shows the 6.7 keV Fe line intensity distribution measured with ASCA GIS (Maeda 1998), convolved with the PIN angular response which is shown by a red triangle.

Furthermore, the PIN count rate varied significantly during this particular pointing (figure 2 bottom).

We consider that a transient source SAX J1747.0−2853, which was outside the XIS FOV but inside that of PIN, caused this discrepancy. According to observations with Chandra, Swift, and INTEGRAL, this transient was in a flaring state since 2005 October (e.g., Wijnands et al. 2005; Kong, Wijnands & Homan 2005; Kuulkers et al. 2007), with an intensity of ~ 10 mCrab in the $20 - 60$ keV band (Kuulkers et al. 2007). It further brightened up to ~ 20 mCrab during our Region C observation, according to the INTEGRAL IBIS monitoring data (Kuulkers et al. 2007).

In the estimation of the bright point source contributions (§5.2), we scaled the power-law model of SAX J1747.0−2853 to the $20 - 60$ keV intensity of 20 mCrab reported by IBIS. However, even after this subtraction, the Region C counts remained unusually high (figure 10). Supposing that the proper Region C brightness is comparable to that of Region A, the excess in figure 10 can be explained if SAX J1747.0−2853 was during the Region C observation twice as bright (~ 40 mCrab) as the week-averaged IBIS intensity. Such a variation is reasonable for transient LMXBs.

5.4. *Comparison with the ridge and bulge emission*

The extended X-ray emission, accompanied by a hard tail, has been observed by many investigators from the Galactic ridge and bulge regions. The spectrum is described by one or two thermal component(s) plus a power-law tail; e.g. $kT = 3.1 \pm 1.4$ keV and $\Gamma = 1.58 \pm 1.05$ in the Galactic ridge region (Yamasaki et al. 1997), while $kT \sim 3$ keV and $\Gamma \sim 1.8$ in the Galactic bulge (Kokubun 2001). In both cases, the thermal and power-law components cross are inferred over at $\sim 6 - 8$ keV in the spectrum. It is remarkable that the two regions exhibit very similar spectra, in spite of different interstellar environments.

The present Suzaku studies have for the first time clarified that such a hard-tail component also accompanies the extended GC emission; it underlies the thermal emission in the XIS band, and carries a dominant flux in the HXD-PIN band. When

this component is represented by a cutoff power-law model, it is inferred to cross with the thermal component at an energy of ~ 7 keV (figure 9). This crossing energy is very close to those found in the other two regions, implying a close similarity among the extended X-ray emissions from the three distinct spatial components.

According to Valinia et al. (2000), the $10 - 400$ keV hard X-ray spectrum of the Galactic ridge emission obtained with the CGRO OSSE is represented better by a cutoff power-law model ($\Gamma = 0.63 \pm 0.25$, $E_c = 41.4^{+13.0}_{-8.4}$ keV), than by a single power law. This appears similar to our cutoff power-law modeling of the GC hard X-rays. However, some caution is needed in this analogy, because the cutoff power-law model reached by Valinia et al. (2000) and that from the present work have quantitatively rather different slopes, becoming discrepant by a factor of ~ 8 at 40 keV, when they are equalized at 10 keV. A more quantitative comparison must await observations of the GC emission over still wider energies.

5.5. *Thermal interpretation of the hard X-ray emison*

After the work by Valinia et al. (2000), Krivonos et al. (2007) argued that the hard X-ray ridge spectrum, with a mildly convex shape, may be interpreted as high temperature thermal bremsstrahlung. Then we also tried to reproduce the Region A spectra with a model consisting of two CIE plasma components and three gaussian lines (hereafter 2T model). The two CIE components were assumed to suffer a common absorption by 6×10^{22} cm^{-2}, and were constrained to have the same (but free) metal abundances. The model reproduced the spectrum well with $\chi^2_\nu = 1.12$ (736), as presented in figure 9d. The two CIE temperatures were obtained as $3.7^{+0.8}_{-0.2}$ keV and $17.8^{+1.0}_{-0.7}$ keV, while the Fe and Ni abundances as $0.81^{+0.03}_{-0.02}$ and $2.0^{+0.3}_{-0.3}$ solar, respectively. The best fit parameters are listed in table 7. Although the ionized iron lines have been explained successfully by Koyama et al. (2007a) using a single CIE plasma with a temperature of $5 - 7$ keV, the present 2T model explains them equally well as a superposition of the cooler and hotter CIE components, which mainly account for the He-like and H-like lines, respectively.

The hotter CIE component implied by the above 2T fit has such a high temperature (17.8 keV). As argued by Krivonos et al. (2007), the temperature would be interpreted easily if the extended hard X-ray emission is composed of a numerous high-temperature thermal point-like sources, such as magnetic CVs. In particular, intermediate polars are good candidates, because their thermal emission sometimes becomes as hot as several tens of keV (Lamb & Masters 1979). Furthermore, this interpretation is consistent with the existence of the strong fluorescent Fe K lines visible in our XIS spectra, because CVs (both magnetic and non-magnetic) are generally known to emit these lines as well (Mukai & Shiokawa 1993; Ezuka & Ishida 1999; Rana et al. 2006).

Although the CV interpretation of the hard component would thus appear plausible, it is at the same time subject to several problems. For example, in order to explain the very constant distribution of the 6.7 keV vs. 6.9 keV line intensity ratio in the $-0°.4 < l < 0°.6$ region (Koyama et al. 2007a; Nobukawa et al. 2007), the assumed hard point sources must have nearly the same spatial distribution as the cooler CIE

emitter. Yet another difficulty is that the 6.7 keV Fe line intensity of the GC emission as measured with the XIS distributes asymmetrically between $l > 0$ and $l < 0$ (Koyama et al. 2007a), which is absent in that of X-ray point sources down to a $2 - 8$ keV flux of 3×10^{-15}ergs cm^{-2} s^{-1} (Muno et al. 2003). Furthermore, according to the 2T fit, the 6.4 keV Fe K line is inferred to have an equivalent width (EW) of ~ 600 eV against the hotter CIE component, while those of CVs are much smaller ($\sim 50 - 200$ eV; Ezuka & Ishida 1999; Rana et al. 2006). Therefore, we must invoke a separate, or an additional, source of the fluorescent lines from the GC region.

5.6. Non-thermal interpretation of the hard X-ray emission with a partially covered model

The thermal plus cutoff power-law model, fitted simultaneously to the XIS and PIN spectra, yielded a photon index of 0.47 (table 6) and a cutoff energy of 9.9 keV. This small photon index suggests the presence of a highly absorbed component in the spectrum. In addition, the GC region hosts a number of dense molecular clouds, with the line-of-sight absorbing column often exceeding 10^{23} cm^{-2}. Therefore, it is plausible to assume that the strong absorption modifies the incoming continuum of the extended GC emission (either diffuse or point-source assembly), by reprocessing and partially absorbing it. These processes are expected to make the observed spectrum slightly convex, because the continuum in the XIS range will flatten. This idea is consistent with the fact that the PIN spectrum from Region A, where clouds must be more plenty, demands a convex model more strongly than that from Region B (table 5). Such dense clouds will not only change the continuum shape, but will also produce the intense fluorescent lines when they are hit by the hard GC X-rays (regardless of its origin), and/or by other excitation sources such as relativistic particles (Bykov 2002), or past activity of the GC black hole (Koyama et al. 1996). Actually, dense molecular clouds are known to emit intense 6.4 keV Fe Kα line (Koyama et al. 1996).

In order to examine whether the mild spectral cutoff seen in the PIN energy band can be explained by the presence of dense interstellar molecular clouds, we introduced an alternative model to fit the combined spectra of Region A. It is the same as Model (b) of section 4.6 (consisting of a CIE model, three gaussians, and a power-law tail), but all the model components are now subjected to a partially-covered absorption (using wabs). That is, a certain fraction f (left free to vary) of the overall spectral model is assumed to be absorbed only by $N_{\rm H} = 6 \times 10^{22}$ cm^{-2}, while the rest, $(1 - f)$, is covered additionally by a thicker column of $N_{\rm H}^*$. For the same reason as in §4.6, we fixed the Fe abundance of the CIE plasma model to 1.0 solar, and furthermore, $N_{\rm H}^*$ to a representative value of 30×10^{22} cm^{-2} because it is not well constrained. As shown in figure 9e, this model has indeed given an equally acceptable fit as the 2T model, with $\chi^2_\nu = 1.14$ (736). The determined plasma temperature and photon index are $6.1^{+0.2}_{-0.1}$ keV and $2.31^{+0.03}_{-0.03}$, while the non-covered fraction is $f = 0.56^{+0.05}_{-0.13}$. The best fit parameters are listed in table 7. We repeated the fitting by changing $N_{\rm H}^*$ over $(10-50) \times 10^{22}$ cm^{-2}, and obtained qualitatively the same results.

The EW of the 6.4 keV Fe line emission turned out to be $\sim$

Table 7. Results of simultaneous fits to the XIS and residual PIN spectra of Region A with the 2T model and the partially covering model.*

	(d) 2T[†]	(e) P.C.[†]
$N_{\rm H}$ (cm^{-2})	6×10^{22} (fix)	6×10^{22} (fix)
$N_{\rm H}^*$ (cm^{-2})	—	30×10^{22} (fix)
$N_{\rm Fe}$ (cm^{-2})	$8.8^{+0.9}_{-1.0} \times 10^{18}$	$8.0^{+0.8}_{-0.8} \times 10^{18}$
Thermal		
kT_1 (keV)	$3.7^{+0.8}_{-0.2}$	$6.1^{+0.2}_{-0.1}$
$Z_{\rm Fe}$ (solar)	$0.81^{+0.03}_{-0.02}$	1.0 (fixed)
$Z_{\rm Ni}$ (solar)	$2.0^{+0.3}_{-0.3}$	$2.1^{+0.4}_{-0.4}$
Redshift	$1.31^{+0.03}_{-0.15} \times 10^{-3}$	$1.9^{+0.1}_{-0.1} \times 10^{-3}$
Norm.$_1$[‡]	$4.33^{+0.16}_{-0.12}$	$2.56^{+0.13}_{-0.04}$
kT_2 (keV)	$17.8^{+1.0}_{-0.7}$	—
Norm.$_2$[‡]	$3.36^{+0.12}_{-0.21}$	—
Emission lines		
Fe I[§] Kα		
$E_{\rm center}$ (eV)	6402^{+1}_{-1}	6400^{+2}_{-2}
σ (eV)	< 11	< 6
Intensity[‖]	$3.50^{+0.05}_{-0.10} \times 10^{-2}$	$4.94^{+0.06}_{-0.05} \times 10^{-2}$
Fe I[§] Kβ		
$E_{\rm center}$[#] (eV)	7061	7059
σ[#] (eV)	< 12	< 7
Intensity[‖]	$4.7^{+0.4}_{-0.4} \times 10^{-3}$	$3.6^{+0.3}_{-0.3} \times 10^{-3}$
Ni I[§] Kα		
$E_{\rm center}$ (eV)	7482^{+20}_{-19}	7479^{+19}_{-19}
σ (eV)	0 (fix)	0 (fix)
Intensity[‖]	$1.8^{+0.4}_{-0.4} \times 10^{-3}$	$1.4^{+0.4}_{-0.3} \times 10^{-3}$
Hardtail		
Γ	—	$2.31^{+0.03}_{-0.03}$
Norm.**	—	$2.39^{+0.06}_{-0.08}$
Constant	$0.39^{+0.01}_{-0.01}$	$0.39^{+0.01}_{-0.01}$
f[††]	—	$0.56^{+0.05}_{-0.13}$
$\chi^2_\nu\,(\nu)$	1.12 (736)	1.14 (736)

*Errors are at 90% confidence level.
[†]2T : two thermal plasma emission plus three gaussian lines. P.C. : a thermal emission model with a power-law tail partially covered with a dense absorbing matter.
[‡]$10^{-14}/(4\pi D^2) \int n_{\rm e} n_{\rm H} dV$, where D is the distance to the source (cm), $n_{\rm e}$ and $n_{\rm H}$ are the electron and hydrogen density in cm^{-3}, respectively.
[§]Or in low ionization states.
[‖]In units of photons s^{-1} cm^{-2}.
[#]Fixed at $1.103 \times E_{\rm center}$(Fe I K$\alpha$) and $1.103 \times \sigma$(Fe I Kα).
**In units of photons s^{-1} cm^{-2} keV^{-1} at 1 keV.
[††]Fraction of non-covered component in the P.C. model.

540 and ~ 270 eV, against the strongly absorbed continuum and the total (strongly absorbed plus mildly absorbed) continuum, respectively. According to Makishima (1986), reprocessing of a power-law ($\Gamma = 0.8$) emission by a spherically surrounding matter, with a column density of $N_H = 30 \times 10^{22}$ cm^{-2} and cosmic abundance, is expected to produce a fluorescent Fe line with EW~ 300 eV (Model II of Makishima 1986). If the surrounding matter is somehow transparent only toward our line of sight (Model I of the same article), the EW decreases to 200 eV. In the present case, the direct and strongly absorbed components are mixed with the fraction f, so that the derived EW ($270 - 540$ eV) should be compared with the mixture of the above two cases (300 and 200 eV). Considering that the extended GC emission has a spectral shape different from the power law ($\Gamma = 0.8$) assumed in Makishima (1986), and that the molecular clouds in the GC region may be richer in heavy elements, the agreement (within a factor of ~ 2) is considered tolerable.

Introducing the above partial-covering model, we have successfully reconciled the mildly curving PIN spectra with the results from the detailed plasma diagnostics, obtained by Koyama et al. (2007a) using the same XIS data. Specifically, the CIE plasma model can be attributed to thermal emission from a truly diffuse hot plasma filling the GC region; in particular, the obtained CIE temperature agree with that derived by Koyama et al. (2007a). The power-law hard tail with $\Gamma = 2.3$ can be comfortably interpreted as diffuse non-thermal emission from accelerated non-thermal or supra-thermal electrons, as argued for the ridge emission by, e.g., Yamasaki et al. (1997), Dogiel et al. (2002), and Masai et al. (2002), and for the bulge emission by Kokubun (2001). The value of f implies that the covered and uncovered fractions are roughly comparable, in agreement with our picture invoking the diffuse hard-tail emitter intermixed with molecular clouds.

References

Bélanger, G., et al. 2004, ApJ, 601, L163

Bykov, A. M. 2002, A&A, 390, 327

Courvoisier, T. J.-L., et al. 2003, A&A, 411, L53

Cremonesi, D. I., Mereghetti, S., Sidoli, L., & Israel, G. L. 1999, A&A, 345, 826

Del Santo, M., Sidoli, L., Bazzano, A., Cocchi, M., De Cesare, G., Paizis, A., & Ubertini, P. 2006, A&A, 456, 1105

Dogiel, V. A., Inoue, H., Masai, K., Schönfelder, V., & Strong, A. W., 2002, ApJ, 581, 1061

Ebisawa, K., Bourban, G., Bodaghee, A., Mowlavi, N., & Courvoisier, T. J.-L. 2003, A&A, 411, L59

Ebisawa, K., Maeda, Y., Kaneda, H., & Yamauchi, S. 2001, Sci., 293, 1633

Ezuka, H., & Ishida, M. 1999, ApJS, 120, 277

in't Zand, J. J., Heise, J., Brinkman, A. C., Jager, R. et al. 1991, Adv. Space Res., 11, 187

Iwan, D., Marshall, F. E., Boldt, E. A., Mushotzky, R. F., Shafer, R. A., & Stottlemyer, A. 1982, ApJ, 260, 111

Kaneda, H., Makishima, K., Yamauchi, S., Koyama, K., Matsuzaki, K., & Yamasaki, N. Y. 1997, ApJ, 491, 638

Kokubun, M. 2001, PhD thesis, The University Of Tokyo, ISAS research note No.823

Kokubun, M., et al. 2007, PASJ, 59, S53

Kong, A. K. H., Wijnands, R., & Homan, J. 2005, ATEL, 641

Koyama, K., Awaki, H., Kunieda, H., Takano, S., Tawara, Y., Yamauchi, S., Hatsukade, I., & Nagase, F. 1989, Nature, 339, 603

Koyama, K., et al. 2007a, PASJ, 59, S245

Koyama, K., Maeda, Y., Sonobe, T., Takeshima, T., Tanaka, Y., & Yamauchi, S. 1996, PASJ, 48, 249

Koyama, K., Makishima, K., Tanaka, Y., & Tsunemi, H. 1986, PASJ, 38, 121

Koyama, K., et al. 2007b, PASJ, 59, S23

Koyama, K., et al. 2007c, PASJ, 59, S237

Krivonos, R., Revnivtsev, M., Churazov, E., Sazonov, S., Grebenev, S., & Sunyaev, R., 2007, A&A, 463, 957

Kuulkers, E., et al. 2007, A&A, 466, 595

Lamb, D. Q., & Masters, A. R. 1979, ApJ, 234, L117

Lewin, W. H. G., Hoffman, F. A., Doty, F., Hearn, D., R., Clark, G. W., Fernigan, F. G., Li, F. K., McClintock, F. E., & Richardson, F. 1976, MNRAS, 177, 83

Maeda, Y., 1998, PhD thesis, Kyoto University, ISAS research note No.653

Makishima, K., 1986, in The Physics of Accretion onto Compact Objects, ed. K. O. Mason, M. G. Watson and N. E. White (Berlin: Springer-Verlag) 249

Masai, K., Dogiel V. A., Inoue, H., Schönfelder, V., & Strong, A. W. 2002, ApJ, 581, 1071

Mitsuda, K., et al 2007, PASJ, 59, S1

Muno, M. P., Baganoff, F. K., Bautz, M. W., Brandt, W. N., Broos, P. S., Feigelson, E. D., Garmire, G. P., Morris, M. R., Ricker, G. R., & Townsley L. K. 2003, ApJ, 589, 225

Muno, M. P., Baganoff, F. K., Bautz, M. W., Feigelson, E. D., Garmire, G. P., Morris, M. R., Park, S., Ricker, G. R., & Townsley L. K. 2004, ApJ, 613, 326

Mukai, K., & Shiokawa, K. 1993, ApJ, 418, 863

Neronov, A., Chernyakova, M., Courvoisier, T. J.-L., & Walter, R. 2005, arXiv:astro-ph/0506437

Nobukawa, M., et al. 2007, PASJ, submitted

Porquet, D., Rodriguez, J., Corbel, S., Goldoni, P., Warwick, R. S., Goldwurm, A., & Decourchelle, A. 2003, A&A, 406, 299

Rana, V. R., Singh, K. P., Schlegel, E. M., & Barreti P. E. 2006, ApJ, 642, 1042

Revnivtsev, M., & Sazonov, S. 2007, arXiv:astro-ph/0702640

Revnivtsev, M., Sazonov, S., Gilfanov, M., Churazov, E., & Sunyaev, R. 2006, A&A, 452, 169

Sakano, M., Koyama, K., Murakami, H., Maeda, Y., & Yamauchi, S. 2002, ApJS, 138, 19

Sugizaki, M., Mitsuda, K., Kaneda, H., Matsuzaki, K., Yamauchi, S., & Koyama, K. 2001, ApJS, 134, 77

Sidoli, L., & Mereghetti, S. 1999, A&A, 349, L49

Sidoli, L., Mereghetti, S., Israel, G. L., Chiappetti, L., Treves, A., & Orlandini, M. 1999, ApJ, 525, 215

Takahashi, T., et al. PASJ, 59, S35

Valinia, A., Kinzer, R. L., & Marshall, F. E. 2000, ApJ, 534, 277

Valinia, A., & Marshall, F. E. 1998, ApJ, 505, 134

Warwick R. S., Turner M. J. L., Watson M. G., & Willingale R. 1985, Nature, 317, 218

Worrall, D. M., Marshall, F. E, Boldt, E. A., & Swank, J. H. 1982, ApJ, 255, 111

Wijnands, R., et al. 2005, ATEL, 637

Yamasaki, N. Y. et al. 1997, ApJ, 481, 821

Yamauchi, S., Kawada, M., Koyama, K., Kunieda, H., Tawara, Y., & Hatsukade, I. 1990, ApJ, 365, 532

Yamauchi, S., & Koyama, K. 1993, ApJ, 404, 602